MSDE

REVIEW

View Article Online
View Journal | View Issue

Cite this: *Mol. Syst. Des. Eng.*, 2023, **8**, 151

Metal–organic framework-derived semiconductors for photocatalytic hydrogen production

Emmanuel Nyela Musa and Kyriakos C. Stylianou *

Received 15th October 2022,
Accepted 7th December 2022

DOI: 10.1039/d2me00221c

rsc.li/molecular-engineering

Hydrogen production as a green renewable fuel using photocatalysis is a viable approach that can realize a near-zero emission from clean energy consumption while promoting environmental sustainability. Metal–organic frameworks-derived semiconductors (MOF-SCs) have emerged as promising candidates to drive this technology due to the unique intrinsic properties they can acquire from the parent MOFs through careful design and synthesis, making them highly attractive for energy and environmental applications. MOF-SCs have shown great potential for simultaneous energy production and environmental remediation, referred to as dual-functional photocatalysis (DFP). However, only a little is understood about how to maximize their activity for efficient performance in DFP. Herein, we describe different strategies associated with the design, synthesis, and application of MOF-SCs for hydrogen production and provide insights into their potential for DFP, which is considered a sustainable way of maximizing the photocatalytic system.

Design, System, Application

Most traditional semiconductors such as metal oxide salts are commercially available with wide applications in energy and technology. However, their application in photocatalysis is largely limited to their surface which serves as the interphase between the reactant and the catalyst. Metal–organic framework (MOF) derived semiconductors (MOF-SCs), however, possess excellent properties relative to their counterparts' traditional semiconductors such as templated porosity, defects, high surface area, high concentration of oxygen vacancies, and a distinct structural morphology, which they can acquire from the parent MOF, making them attractive candidates for heterogeneous photocatalysis. In our review, we describe the design, synthesis, engineering and photocatalytic activity of MOF-SCs for hydrogen production. We also report their use in dualfunctional photocatalysis for generating hydrogen while organic substances are degraded. This process is sustainable and can maximize the full potential of the photocatalytic system, thus promoting high energy conversion and environmental remediation.

Introduction

The over-reliance on non-renewable energy resources, such as fossil fuels, accompanied by their current inadequate supply, has plunged the world into a global energy crisis. Moreso, the effects of the consumption of these energy resources are contributing to climate and environmental changes, pushing the threshold level higher and exerting immense pressure on our ecosystem and the world's economy. Besides, the deposits of these non-renewable resources are gradually depleting, resulting in an upsurge of alternative renewable energy resources such as hydrogen.[1,2] Hydrogen fuel has been considered a suitable candidate and a clean green energy carrier whose production can be actualized from renewable sources,[3,4] however, the technology is grossly limited due to cost. The cost of hydrogen fuel production is targeted at $2 per kg by 2025 and $1 per kg by 2030 by the US department of energy.[5] Hydrogen can be produced by employing different approaches such as steam methane reformation,[6] water electrolysis,[4] and photocatalysis.[7] Out of these approaches, photocatalysis has been considered a suitable technology that can drive high energy conversion by utilizing the earth's abundant solar energy in the presence of a photoactive catalyst to generate hydrogen from water splitting,[1] owing to the abundant nature of water, and its rich proton source.

The first attempt at water splitting dates back to 1972 when Fujishima and Honda performed the electrochemical photolysis of water using the photocatalysts TiO_2 as a semiconductor (SC) electrode.[8] This breakthrough birthed many interests in the quest for highly efficient catalysts in design, synthesis, and development for heterogeneous photocatalytic applications. Apart from the photocatalytic water splitting into H_2 and O_2, otherwise called the hydrogen evolution reaction (HER) and oxygen evolution reaction (OER), photocatalysis has also attracted wide application in

Materials Discovery Laboratory (MaD Lab), Department of Chemistry, Oregon State University, Corvallis, Oregon 97331, USA.
E-mail: kyriakos.stylianou@oregonstate.edu

other areas such as (i) CO_2 reduction,[9] (ii) oxidation of organic molecule into value-added products and their removal from the environment, usually as a form of wastewater treatment,[10] and (iii) metal reduction.[11] Many traditional SCs, such as TiO_2,[8,12] ZnO,[13,14] MnO_2,[15,16] Fe_2O_3,[17] and Bi_2O_3–ZnO,[18] have shown great potential for photocatalytic applications owing to their light absorption ability, chemical and thermal stability, cost-efficiency, and low toxicity.[13,19,20] Despite these remarkable properties, using SCs as photocatalysts has faced many setbacks, some of which are still being researched extensively for improvement, practicality, and industrial scalability. The major challenges associated with most traditional SCs photocatalysts have been primarily attributed to the following factors (i) narrow operation in the UV region, which accounts for less than 5% of the broad electromagnetic spectrum[1,21] and (ii) high electron–hole pair recombination during reactions.[22,23] Thus, there is a need to develop novel materials and technologies to promote the production of renewable H_2 fuel. The application of MOFs and MOF-derived SCs for hydrogen production has been summarized in the literature. Our group and others have recently summarized the dual functional photocatalysis of MOFs for hydrogen production and oxidation of organic molecules[11,24] Wen *et al.* summarized the design and synthesis of metal–organic frameworks for visible light-enhanced hydrogen production.[25] Xu *et al.* summarized MOF-based catalysts for hydrogen.[26] Lelu summarized MOF-derived heterojunctions for hydrogen production.[27] Herein, we overview the design and generation of MOF-derived SCs for hydrogen production. We also outline the important precedents that contributed to the body of work and the current state of research, and their potential application for dual functional photocatalysis.

Photocatalytic water splitting

The principle of photocatalysis for water splitting is widely understood and proceeds as follows; (i) the photocatalyst absorbs sufficient energy upon light irradiation, followed by the generation of charged species (electrons and holes), the diffusion of the electrons to the active sites on the conduction band (CB) occurs, leaving the holes localized in the valence band (VB), and (iii) the subsequent production of H_2 through water reduction (HER) by the electrons,[11,28,29] with minimal interference from the holes in the VB. The HER also requires that the CB of the SC photocatalyst is more negative than the hydrogen reduction potential (E^0 H^+/H_2 0.00 V *vs.* SHE). Thus, the reaction proceeds uphill with a high Gibbs free energy change of 237.13 kJ mol^{-1} and requires photons with energy higher than 1.23 eV to drive the process.[27] However, the HER is often staggered due to the high recombination rate of the photogenerated charged holes in the VB and electrons in the CB needed to drive the reaction.[23] To maximize the hydrogen evolution rate, organic solvents such as methanol, ethanol, and TEA are often employed as sacrificial electron donors and used as scavengers to trap the photogenerated holes while replenishing the deficient electrons in the system, thus allowing better mobility of the electrons to the active sites of the SC photocatalyst,[30] a means of promoting charge transfer. Sacrificial electron donors can improve the efficiency of the photocatalyst for higher hydrogen evolution rates. However, their industrial application is inhibited due to costs and the potential to cause secondary poisoning to the system.[31,32] Noble metal co-catalysts, such as Pt, Pd, and Au nanoparticles,[2,33] have been employed to overcome the activation energy barrier for higher hydrogen evolution rates, but the cost of these noble metals limits their industrial usage. Non-noble metals have also been employed as alternative co-catalysts[34,35] to the expensive noble metals, however, HER still suffers low production rates. Other approaches involving the engineering and design of the SC include the creation of heterojunctions,[36] and doping with non-metals[37,38] which can potentially narrow the wide band gaps of the SCs, thus promoting a better charge transfer process and reducing the high recombination rates of photogenerated species. As the quest for efficient SCs for photocatalytic application continues, the last decade has seen many approaches, one of which involves the use of metal–organic frameworks (MOFs) as precursors for synthesizing MOF derivatives, such as MOF-derived SCs. MOF-5 was first employed as a precursor to porous carbons, which was applied as an electrode for supercapacitors in 2010.[39,40] The design of these materials has gained wide interest and ever since, and different MOF derivatives have been formulated for different applications.

Metal–organic frameworks as sacrificial reagents for the formation of semiconductors

MOFs have been considered excellent candidates in photocatalysis.[41–43] This is due to their many advantages, such as their three-dimensional porous frameworks, structural tunability, crystallinity, high surface area, and short diffusion lengths of charge carriers.[24,44] Despite these unique properties, many MOFs suffer from poor stability both in solution and under accelerated temperatures, rendering their application in photocatalysis limited.[25,45] However, the properties of MOFs are highly desired for photocatalysis, and interestingly, they can be carefully tailored into MOF-derived semiconductors (MOF-SCs), metal nitrides, and metals,[40] imparting stability and some degree of performance over the MOF derivatives. While the library of available MOFs is inexhaustible, only a few, such as MOF-5, MOF-74, UiO-66, the MILs-125-NH_2, and the ZIF (ZIF-8, ZIF-67), have shown great promise as templates for the generation of MOF-derivatives.[46] MOF-SCs can inherit some unique properties of the parent MOFs such as the templated morphology, porosity, surface area, and crystallinity, enhancing their photocatalytic activity for improved

performance.[47] MOF-derived templates have shown merits and proven to be viable for extending the bandwidth of MOFs for an array of other applications such as electrode materials,[48] photoanodes for dye-sensitized solar cells panels,[49,50] photocatalysis,[7,51,52] and in electrocatalytic and photoelectrocatalytic applications.[53,54] Also, the careful design and synthesis of MOF-derivatives can address some of the posing challenges associated with the high recombination rate of photogenerated charged species, thus eliminating the use of poisonous sacrificial electron donors and expensive noble metal co-catalysts, making them promising candidates for HER.

The synthesis of MOF-SCs must be done to ensure that the unique desired properties of the parent MOFs are carefully tailored to the SCs. Because MOFs are highly tunable with extended 3-dimensional networks, the advantages of their versatility allow an immense degree of control during the engineering of the MOF-SCs. Many considerations must therefore be taken into the design and synthesis of the MOF-SCs for better-improved performances. During the synthesis of MOF-SCs, important properties such as the crystal size, structural morphology, chemical composition, weight, and atomic percentages of the resultant crystal phases can be related to the calcination or annealing process,[55] contributing to the overall performance of the MOF-SCs in photocatalysis. Engineering defects and doping MOF-SCs with nonmetals have also been shown to increase their overall performance. In addition, the formation of heterojunctions from the combination of two or more MOFs has also been adapted to address the high recombination rates of photogenerated charged species for better separation of charged species and to promote faster migration of the electrons, usually to the active sites of MOF-SCs during photocatalysis.[18,56] Herein, we describe some of these strategies employed in the design and synthesis of MOF-SCs, and how they impact their performance in photocatalysis.

1. Optimization of the calcination time, temperature, and environment. MOF-SCs are obtained when MOFs are pyrolyzed. During the process, the extended framework of the MOF collapses wholly or partially. The calcination time and environment chosen tend to impart the formation of various products, such as metal oxides or metal nanoparticles on carbon, depending on whether it is done under inert or air conditions. Calcination at higher temperatures could also result in the formation of different phases of SCs. Additionally, the heating and cooling rates are crucial factors in tailoring these useful properties to the MOF SCs. Therefore, one must decide on the product of interest and ensure that careful measures are followed during the calcination process, as all these parameters play key roles in the activity of the MOF-SC. Hussain *et al.* synthesized different $TiO_2/Cu_xO/C$ composites from a bimetallic MOF, NH_2-MIL-125(Ti/Cu), for hydrogen production, by varying different synthesis conditions such as the pyrolysis time and temperature, as a function of the increased activity of the catalysts.[57,58] Results from their experiments showed that the MOF-derived $TiO_2/Cu_xO/C$ with dwell times of 0.5 and 4 h under 700 °C, exhibited different HER activities, and was attributed to the fact that the pyrolysis time of the MOF-template employed, determined the crystallinity of the derivatives. The textural properties of the porous carbon in the resulting composites, consequently affecting the HER performance.[58] Kampouri *et al.* explored the effect of different calcination temperatures on the synthesis of mixed-phase anatase/rutile heterojunction from a Ti-MOF MIL-125-NH_2 (Fig. 1).[7] Their results indicated that the gradual decomposition of the MOF framework manifested into the amorphous phase TiO_2, derived at 400 °C, to the metastable single phase anatase at 500 °C.

Upon further calcination to 600 °C, the mixed anatase/rutile heterojunction manifested and transformed fully to the highly crystalline single rutile phase at 800 °C. It was observed that the calcination temperature imparted the composition of TiO_2 as the temperature varied, yielding different ratios of anatase/rutile mixtures. L. Pan and co-workers reported the generation of C-doped ZnO from a ZIF-8 MOF using a two-step calcination process.[51] The MOF was first calcined at 350 °C for 2 h at a heating rate of 5 °C min^{-1}, and then, the temperature was increased to 400/450 °C at a heating rate of 2 °C min^{-1} and maintained for 1 h. They showed that the crystallinity, morphology, and size of the ZnO SC formed were largely affected by varying the time and the calcination temperature.[51] Zhao *et al.* reported a new type of ZnO/ZnS nanostructures fabricated by coupling solvothermal synthesis with a two-step calcination strategy of MOF-5 and thioacetamide, in which they showed that by controlling the calcination time and temperature, the interfacial catalytic active sites were improved.[59] Moreso, a recent study by Bhadra *et al.* indicated that MOFs pyrolyzed at a temperature higher than 350 °C tend to lose their well-ordered crystalline structure transforming the metal centers into metal compounds and converting the organic linkers into amorphous carbon matrices.[60] Regarding the impact of the calcination atmosphere on the MOF SCs, Das and co-workers earlier reported that metal ions with a reduction potential of −0.27 V and above, such as those of Co, Cu, and Ni with a +2 charge, often form pure metal nanoparticles upon pyrolysis under inert atmosphere, while those with reduction potential below −0.27 V, such as Ti^{4+}, Fe^{3+}, and Al^{3+}, formed metal oxides upon reacting with the oxygen from the organic linkers in the MOF.[61] This is advantageous because the single or pure metal nanoparticles formed from the inert calcination process can be used as co-catalysts, to enhance the photocatalytic activity due to their degrees of freedom within the MOF-derivative, allowing them to interact, and contribute to the concentration of active sites, thus eliminating the requirement for noble metal co-catalysts. Overall, understanding the impact of these parameters will allow the careful architecture of the resulting MOF-SCs. Additionally, the choice of the MOF used will play a crucial role in the MOF-derivative formed.

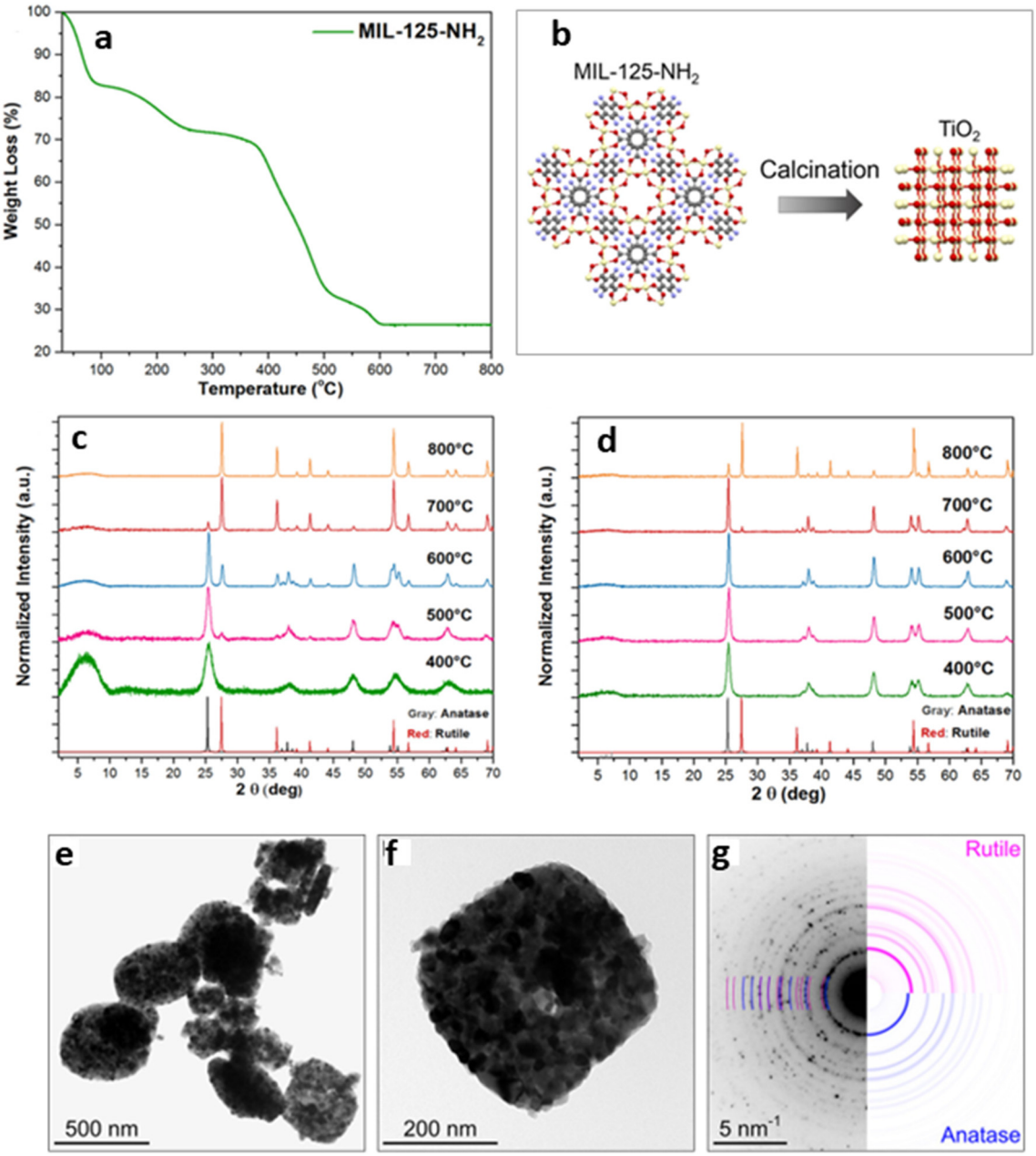

Fig. 1 (a) TGA curve of MIL-125-NH_2. (b) Schematic showing the synthesis of MIL-125-NH_2-derived TiO_2. PXRD patterns of the as-synthesized (c) MIL-125-NH_2-derived and (d) TiH_4O_4-derived. (e) and (f) Bright-field TEM images of MIL-125-NH_2, and (g) selected area electron diffraction pattern of MIL-125-NH_2-derived TiO_2.[7]

2. Engineering of defects on MOF-derived semiconductors: oxygen vacancies are the most reported defects associated with semiconductors, and careful engineering can tune the functional properties of metal oxides, such as charge transport, electronic structure, and catalytic performance.[62,63] In MOFs, most defects are caused by the dislocation of atoms, which breaks the regular periodic arrangement in the framework.[64] Basically, defects can be introduced through different methods, one such way is the post-synthetic modification technique, which can develop numerous defects on the MOF.[65] Like the other properties of MOFs, these defects can be transferred to MOF-SCs, by careful pyrolysis. This implies that the photocatalytic performance of the catalyst can be controlled using defects or vacancies. It has been reported in many oxides as they can potentially improve the light absorption capacity, charge carrier separation, and the surface reaction sites of the photocatalyst.[64,65] The presence of dopants like metals, *e.g.*, Cu, Ag, Zn, Mn, and Ni, and nonmetals, *e.g.*, N, S, and P on the SC, can introduce impurities into the lattice of the SC, leading to the creation of defects. Because the feasibility of the photocatalytic process is largely dependent on the band alignment between the CB and VB, doping can therefore improve the performance of the SC by tuning the electronic structure and

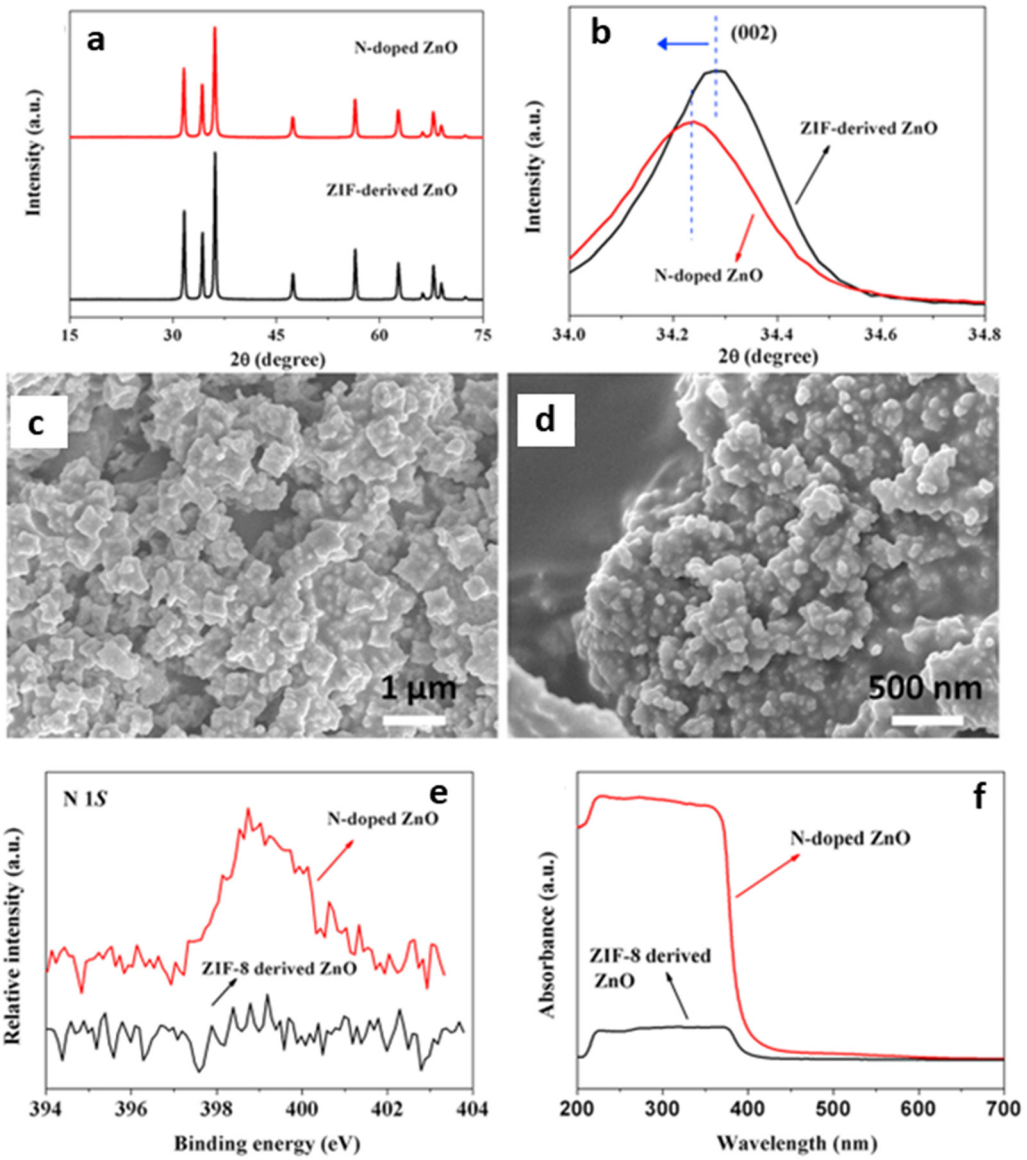

Fig. 2 PXRD patterns of ZIF-8 derived pure ZnO and N-doped ZnO: (a) 2θ between 25° and 75° and (b) 2θ between 34.0° and 34.8°. SEM images of (c) ZIF-8 derived pure ZnO, and (d) N-doped ZnO (e) XPS spectra of N 1s and (f) UV-vis adsorption spectra of ZIF-8 derived pure ZnO and N-doped ZnO.[67]

modifying the band position for extended light absorption towards better utilization of the solar energy, thus increasing the charge carrier separation of the semiconductor.[38,66] Feng *et al.* had earlier reported the synthesis of ZnO and N-doped ZnO using ZIF-8 as the MOF template in the presence of urea as a nitrogen source *via* direct mixing followed by calcination under oxygen (Fig. 2). Their analysis confirmed the successful incorporation of the N atom within the ZnO lattice, resulting in a higher BET surface area than the pristine ZnO. They also reported a higher photocatalytic activity for the N-doped ZnO resulting from the doping, which enhanced visible light harvesting and inhibited the recombination of electron and hole pairs.[67]

3. Engineering MOF-derived semiconductors with heterojunctions: the photogeneration of charged carriers is an important step in photocatalysis, however, the migration of these charged species to the active sites of the catalyst for effective performance is more significant. The ability of the photogenerated species to diffuse effectively depends upon the mobility of the charge carrier, diffusion coefficient, lifetime, length of diffusion, carrier concentration, and charge recombination kinetics.[68] High rate of charge recombination limits many photocatalytic reactions, thus the pyrolysis of bimetallic MOFs can offer some solutions to these challenges, as it often leads to heterojunctions with different CBs and VBs between semiconductors, thus minimizing the recombination rate of charged species and promoting better separation and diffusion of charged carriers.[69] An heterojunction can be the interface between two different semiconductors with unequal band structure, resulting in their band alignments.[70,69]

One of the main advantages of heterojunctions is the synergy that exist between the two metal nodes in the MOF-SC derived from the parent bi-metallic or mixed metal MOF templates, which enhances their catalytic activity compared to MOF-SC derivatives with single metal nodes.[54,72] Heterojunctions can be described based on the nature of their band alignment and how photogenerated holes and electrons are distributed between the two photocatalysts. Heterojunctions are classified as conventional, containing the (type-1, type-II, and type-III),[52,69,73] p–n heterojunctions[74,75] and Z-scheme (Fig. 3).[27,76,77] We can therefore describe how these systems or heterojunctions will operate when light is irradiated on them. In type-I, upon light irradiation leading to the generation of charged species, both the electrons and holes of one photocatalyst can migrate to the other photocatalyst, thus creating electron and hole density, which can result in a high concentration of charged species on the photocatalyst (Fig. 3). This can potentially bring about the saturation of the system and, therefore, a poor photocatalytic activity observed. In type-II, the electrons and holes are well distributed due to their band alignment, with the electrons of one photocatalyst migrating to the CB of the other and the holes of the other photocatalyst migrating to the VB of the first (Fig. 3). This brings about better separation and faster migration of charged species between the two photocatalysts. Similarly, a similar phenomenon in type-II is observed in the p–n heterojunction (Fig. 3). The type-III suffers from a mismatch of bands, which results in the poor separation and migration of charge species; hence not much activity is observed. Furthermore, in the Z-scheme heterojunction, electrons from the CB of one photocatalyst could migrate to the VB of the other, hence increasing the rate of charge recombination (Fig. 3). Therefore, the type II and p–n heterojunctions are well suited and adapted for minimizing the recombination of photogenerated charged species,[27] which is favorable for photocatalytic water splitting. In the design of heterojunctions, it is also important to consider the impact of the concentration of the MOF templates on the final MOF-SC-derived composite. In fact, getting the right molar ratio between the bimetallic MOFs is one of the most crucial steps to synthesizing heterojunctions with enhanced photocatalytic activity. This is highly significant as an excess of one MOF template may cover the surface-active sites of the other in the composite, resulting in the shielding of light absorption, hence decreasing the activity of the photo-induced charged species.[72,78] Recently Li *et al.* constructed TiO_2/Co_3O_4/Ni heterojunction using bimetallic MOFs, MIL-125/ZIF-67 through a post-annealing process at 500 °C for 2 h under an air atmosphere for hydrogen production (Fig. 4).[71] Zhang and co-workers synthesized a TiO_2/CuO heterostructure derived from Ti and Cu mixed metal MOFs (MIL-125 and Cu-BDC) for hydrogen production.[72] Utilizing the power of Femtosecond transient absorption spectroscopy, they found that electrons have been transferred from the photosensitizer $[Ru(bpy)_3]^{2+}$ to the CB of TiO_2, which served as the mediator, collecting the ultra-fast electrons from the photosensitizer at (<150 fs), and depositing them on the CB of CuO serving as

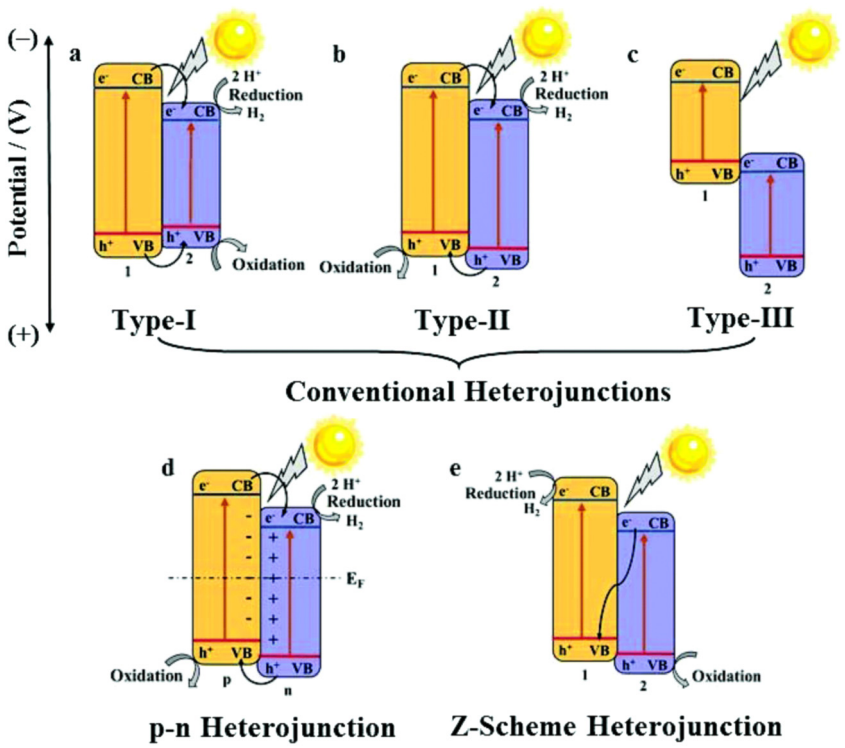

Fig. 3 Diagrams of (a) type-I, (b) type-II, (c) type-III, (d) p–n heterojunction, and (e) Z-scheme heterojunction. 1, 2, p, and n refer to semiconductor 1, semiconductor 2, p-semiconductor, and n-semiconductor, respectively.[27]

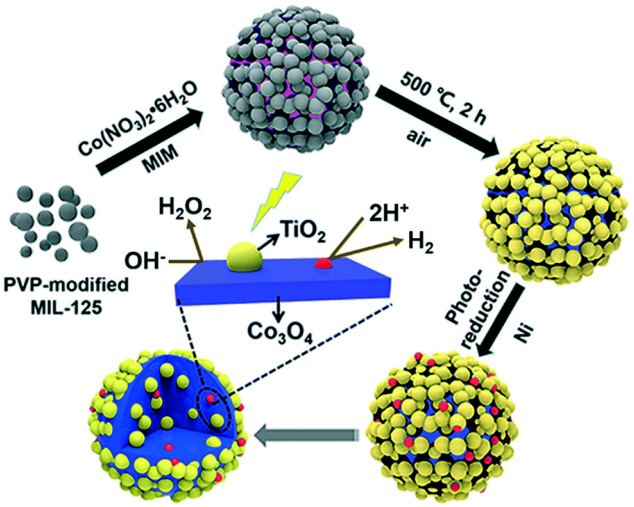

Fig. 4 Schematic illustration for the preparation of TiO_2/Co_3O_4/Ni composites derived from MIL-125@ZIF-67 HMOF.[71]

the cocatalyst where the HER is initiated (Fig. 5). Their reaction mechanism suggested that the electron transfer occurs from $[Ru(bpy)_3]^{2+}$ to TiO_2, resulting in the formation of oxidized $[Ru(bpy)_3]^{2+}$ from quenching of its excited state absorption, followed by injection of the electrons into the CB of TiO_2. They showed that the best activity was observed for the TiO_2/CuO with a 0.4 : 1 molar ratio of Cu and Ti, leading to slower charge recombination due to the long-lived kinetic traces ground state bleach (GSB) that existed for the $[Ru(bpy)_3]^{2+}/TiO_2$ composite.[72] Li *et al.* synthesized a nickel MOF and a cerium MOF, with which they fabricated a NiO/CeO_2 p–n heterojunction by annealing the precursor of the nickel/cerium mixed-metal metal–organic frameworks, resulting in a high-quality interface between the bimetallic NiO/CeO_2 oxide.[52] Zhao and co-workers fabricated a ZnO/ZnS heterojunction for H_2 evolution through the solvothermal synthesis of MOF-5 and coupling with thioacetamide as the source of sulfur.[59] They reported that the ZnO/ZnS nanoparticles were homogeneously integrated, owning to the uniform sulfidation of the MOF precursor, which improved

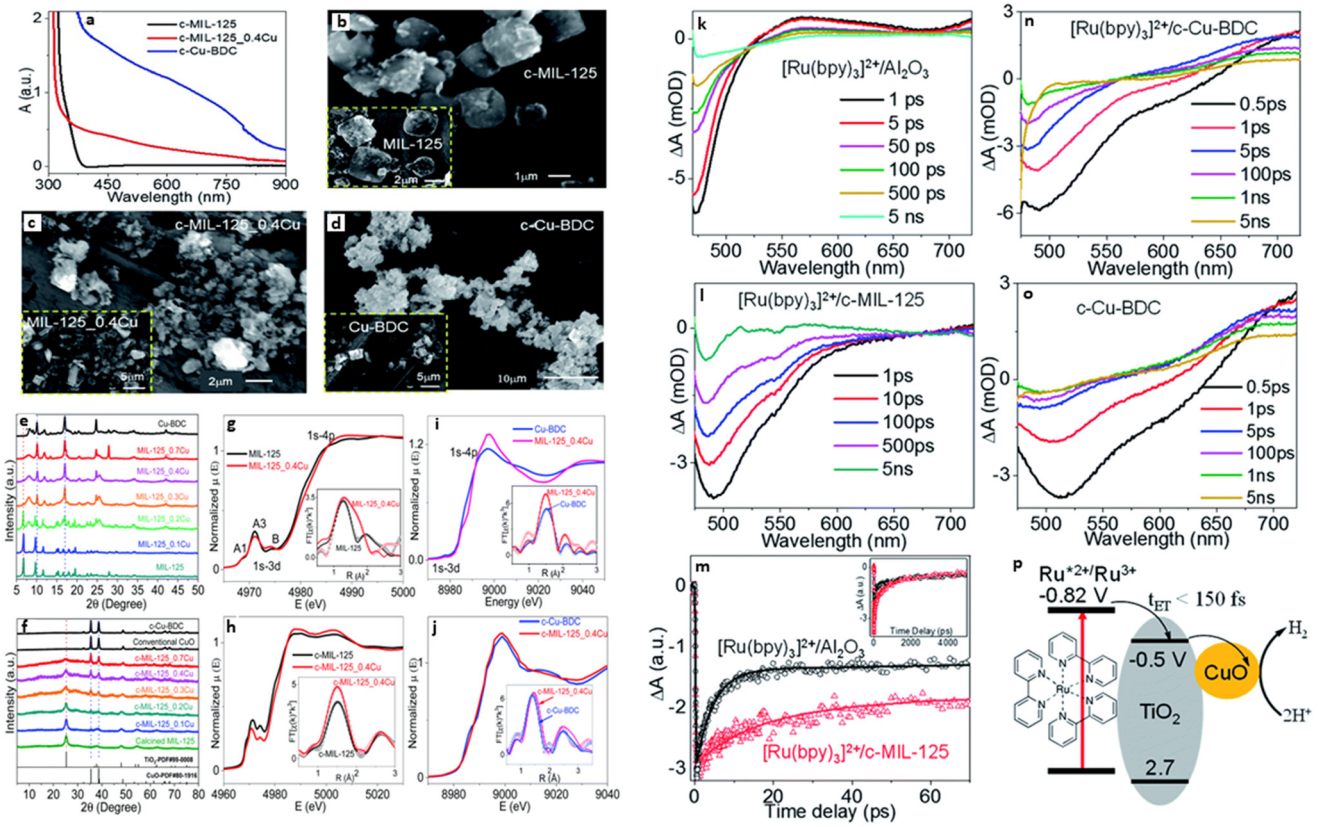

Fig. 5 (a) DRS of c-MIL-125, c-Cu-BDC, and c-MIL-125 0.4 Cu. SEM images of (b) c-MIL-125, (c) c-MIL-125_0.4 Cu, and (d) c-Cu-BDC, as well as their corresponding MOFs before calcination. Powder XRD patterns of (e) MIL-125, Cu-BDC, and MIL-125_*x*Cu (*x* = 0.1–0.7), (f) c-MIL-125, c-Cu-BDC, and c-MIL-125_*x*Cu (*x* = 0.1–0.7), as well as traditional CuO and standard PDF cards of TiO_2 and CuO. XANES spectra and EXAFS spectra in *R*-space with fitting (inset) of (g) MIL-125 and MIL-125_0.4 Cu at the Ti k-edge and (i) Cu k-edge, (h) c-MIL-125 and c-MIL-125_0.4 Cu at the Ti k-edge and (j) Cu k-edge. Transient absorption spectra of (k) $[Ru(bpy)_3]^{2+}/Al_2O_3$, (l) $[Ru(bpy)_3]^{2+}$/c-MIL-125 (n) $[Ru(bpy)_3]^{2+}$/c and (o) Cu-BDC (o), following 450 nm excitation. (m) Comparison of kinetic traces at 500 nm between $[Ru(bpy)3]^{2+}/Al_2O_3$ and $[Ru(bpy)_3]^{2+}$/c-MIL-125, open symbols represent experimental data, and the solid lines represent their best fits. (p) Schematic diagram of the charge transfer process in $[Ru(bpy)_3]^{2+}$/c-MIL-125_*x*Cu, showing potentials *vs.* SCE.[72]

the interfacial catalytic active sites.[59] Using MIL-125-NH_2, Kampouri *et al.* fabricated mixed-phase anatase/rutile MOF-derived TiO_2 nanoparticles for photocatalytic hydrogen evolution.[7] Dekrafft and co-workers synthesized a hematite and anatase phase Fe_2O_3/TiO_2 heterojunction by coating an amorphous shell of titania on Mil-101(Fe) followed by calcination at 550 °C for 16 h.[79] The HER solutions were irradiated using a cut-off filter >420 nm, allowing the passage of visible light. From their results, no H_2 evolution was observed when the HER was performed with Fe_2O_3/TiO_2 in the absence of a sacrificial electron donor and cocatalyst. The inactivity of the HER was associated with the location of the conduction bands of the composite falling below the potential for proton reduction. However, when TEA was employed as a sacrificial electron donor in the presence of Pt, they observed a gradual H_2 evolution of 0.8 μmol g^{-1} h^{-1} after 3 h, which peaked at 30 μmol g^{-1} h^{-1} after 48 h suggesting that TEA and Pt played important roles in the HER. In the absence of TEA, only 0.1 μmol g^{-1} h^{-1} was observed after 3 h. To confirm the roles of TEA and Pt, a series of reactions were carried out using similar conditions, with Fe_2O_3 and TiO_2 individually and with a physical mixing of both. Their results showed that neither of these materials could catalyze the reaction after 3 h, suggesting that Pt was required due to the synergy between the heterojunction and the Pt particles, with TEA as a hole scavenger.[79] MOFs with different metal nodes have also been combined with flexible layered structured graphitic carbon nitride (g-C_3N_4) to form suitable heterojunctions for photocatalysis. While g-C_3N_4 has a narrow energy band gap of (2,5–2.7 eV),[80] it suffers from poor visible light absorption, fast recombination rates of photogenerated charged species, and insufficient active sites for proton reduction.[80,81] However, the combination of g-C_3N_4 with MOF templates results in the formation of MOF-SCs heterojunctions or composites with excellent properties for photocatalytic applications. Recently, Liu and co-workers synthesized a porous In_2O_3/g-C_3N_4 type-II heterojunction using In-MOF and melamine through a hydrothermal annealing process.[82] They found that the derived In_2O_3 was supported on the surface and between the layers of g-C_3N_4, inducing a porosity that provided channels for electrons, resulting in the creation of internal electric fields by the heterostructures, which accelerated the electron transfer process.[82] A series of Z-scheme heterostructures consisting of g-C_3N_4/αFe_2O_3 hybrids were constructed by Liu *et al.* from g-C_3N_4 with various ratios of MIL-101(Fe) through a hydrothermal method for hydrogen production.[83] Results from their analysis showed that the optimized g-C_3N_4/αFe_2O_3 derivative exhibited improved HER activity over the bulk g-C_3N_4 due to the narrow band gaps of the two semiconductors, which enhanced visible light response, and ensured effective separation of photo-excited charge carriers.[83] Using a similar approach, Qi *et al.* synthesized a g-C_3N_4/αFe_2O_3FeP heterojunction from the pyrolysis of g-C_3N_4/Fe-MOF precursors, followed by the phosphidation of the derived MOF-SC using NaH_2PO_2 for enhanced hydrogen evolution.[80] Their experimental results indicated that the HER activity depended on the time of phosphidation and the concentration of eosin Y (EY) acting as the sensitizer in the reaction solution. In the absence of EY, no H_2 was detected for the g-C_3N_4 and Fe_2O_3/g-C_3N_4 composite. However, upon 60 min phosphidation in the presence of 1 mmol EY, the highest H_2 evolution was observed for the derived g-C_3N_4/αFe_2O_3FeP at 12 mmol g^{-1} h^{-1}, 12 times higher than that of the pristine g-C_3N_4 at 0.97 mmol g^{-1} h^{-1}. The increased activity observed for the composites was attributed to the synergistic effect originating from the intimate contact of the Fe_2O_3/g-C_3N_4 heterojunction, along with the presence of electron-capture FeP centers and the presence of the EY sensitizer.[80]

Employing the enhanced separation of photogenerated charge species in heterojunctions for photodegradation reactions, Pi *et al.* synthesized an In_2S_3 hollow tube heterostructure using a multiwalled carbon nanotube encapsulated in MIL-68(In)-(MWCNT@MOF), followed by the sulfidation in thiourea for the degradation of tetracycline, by varying the amount of MWCNT in the composite.[78] The In_2S_3 derived from 0.3%-MWCNT@MOF exhibited the highest photocatalytic activity for TC degradation, with a 100% degradation efficiency more than that observed for pure MOFMOF-derived$_2S_3$. They attributed the high activity observed to the improved visible light response, long transfer, and reduced recombination of charged carriers of the MOF-SC, brought about by the synergy between the MWCNTs and the MOF.[78]

MOF-derived semiconductors for hydrogen production

Photocatalytic water splitting is considered a viable technology in the quest for clean hydrogen fuel generation, and MOF-SCs are key players in the field. MOF-SCs can inherit useful properties from their parent MOFs, such as the templated morphology, crystallinity, surface properties, and porosity with imparted stability. Owing to these promising properties, many researchers have employed MOF-SCs for photocatalytic water splitting and some examples are highlighted in (Table 1). NiO/CeO_2 heterojunction, pure NiO, and CeO_2 were prepared by Li *et al.* from a bimetallic Ni-MOF/Ce-MOF for hydrogen production. Results obtained from their analysis showed a higher photocatalytic performance for the NiO/CeO_2 with H_2 rate of 71 μmol g^{-1} h^{-1} than the single CeO_2 with 4 μmol g^{-1} h^{-1}, while NiO showed no activity for H_2, owing to its relative band gap of 3.43 eV. The increased performance of NiO/CeO_2 was attributed to the fast transfer, and low recombination of charged carriers brought about by an extended optical property and a high-quality interface between the bimetallic MOF SCs.[52] Han *et al.* first synthesized a hexagonal/cubic In_2O_3 Z-scheme phase-junction by directly annealing MIL-68(In)-NH_2 under air at different temperature ranges. The In_2O_3 Z-scheme, formed at 500 °C, exhibited the best

Table 1 Summary of MOF-derived semiconductors for photocatalytic H_2 production

MOF-template	MOF-SC	Synthesis method	Sacrificial agent	Co-catalyst	Activity (μmol g^{-1} h^{-1})	Ref.
MIL-125-NH_2	TiO_2	Solvothermal	Methanol	—	1394	7
Ni-MOF/Ce-MOF	NiO/CeO_2	Solvothermal	—	—	71	52
MIL-125-NH_2/Cu	TiO_2/Cu_xO/C	Ultrasonication	Methanol	—	3298	57
MOF 5/thioacetamide	ZnO/ZnS	Solvothermal	Na_2SO_3, Na_2S	—	415	59
MIL-125/ZIF-67	TiO_2/Co_3O_4/Ni	Solvothermal/photoreduction method	Methanol	Ni	27 000	71
MIL-125-NH_2/Cu-BDC	TiO_2/CuO	Solvothermal	TEOA	—	19 036.2	72
MIL-101(Fe)/titania	Fe_2O_3/TiO_2	Microwave	TEA	Pt	30	79
g-C_3N_4/NH_2-101-Fe/NaH_2PO_2	g-C_3N_4/αFe_2O_3FeP	Solvothermal	TEA	—	1200.3	80
In-MOF/melamine	In_2O_3/g-C_3N_4	Hydrothermal	TEOA	Pt	69	82
g-C_3N_4/MIL-101(Fe)	g-C_3N_4/αFe_2O_3	Hydrothermal	TEOA	Pt	2066	83
MIL-68(In)-NH_2	In_2O_3	Solvothermal	TEA	—	2224	84
TiO_2–Ti_3C_2-ZIF-67	TiO_2/Ti_3C_2/CoS_x	Solvothermal	Methanol	—	9500	85
Cd-Fe-PBA	CdS	Hydrothermal	Na_2S, Na_2SO_3	—	3051.4	86
BiYV-MOF	$Bi_{0.5}Y_{0.5}VO_4$	Ultrasonication/solvothermal	—	Pt	124.2	87

performance giving a hydrogen evolution rate of 2244 μmol g^{-1} h^{-1}, due to an enhanced separation of photogenerated charged species.[84] In_2O_3/g-C_3N_4 type-II heterojunction composites made from an In-MOF and melamine showed improved photocatalytic activity for H_2 evolution with 69 μmol g^{-1} h^{-1}. The authors indicated that the enhancement in the photocatalytic activity was related to the specific surface area, stability, and synergy between the In_2O_3/g-C_3N_4

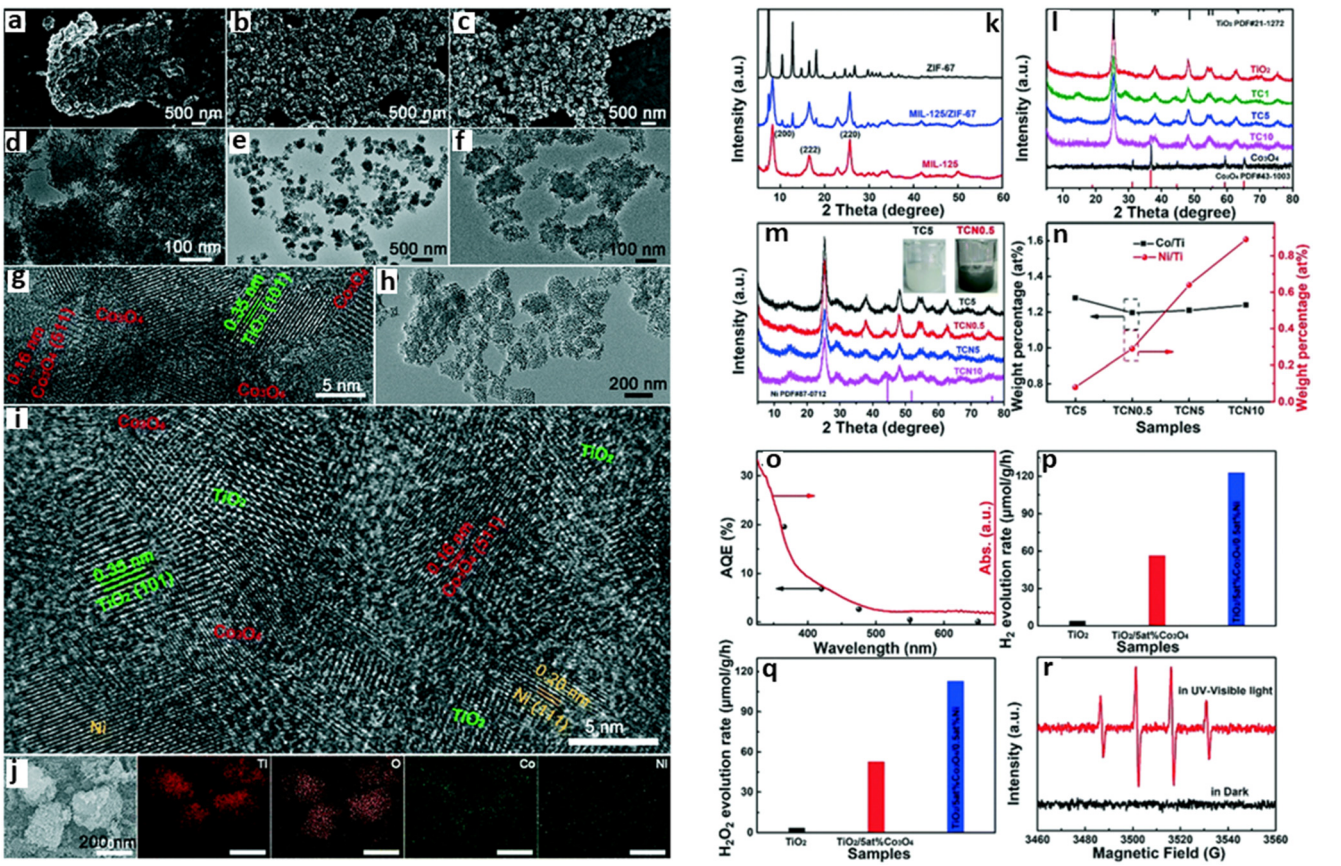

Fig. 6 SEM and TEM images of (a and d) TiO_2, (b and e) MIL-125/ZIF-67, and (c and f) TiO_2/5at%Co_3O_4, and (g) HRTEM image of TiO_2/5at%Co_3O_4. The (h) TEM, (i) HRTEM, and (j) elemental mapping images of TiO_2/5at%Co_3O_4/0.5at%Ni. PXRD patterns of (k) MIL-125, ZIF-67 and MIL-125/ZIF-67, (l) TiO_2, Co_3O_4 and TiO_2/Co_3O_4 heterojunctions and (m) TC5, TCN0.5, TCN5 and TCN10 composite photocatalysts and the color contrast of TC5 and TCN0.5 (inset). (n) ICP-OES experimental data of TC5, TCN0.5, TCN5 and TCN10 samples. (o) Apparent quantum efficiency (AQE) for TiO_2/5at%Co_3O_4/0.5at%Ni at different monochromatic light irradiation wavelengths. The photocatalytic activities of TiO_2, TiO_2/5at%Co_3O_4, TiO_2/5at%Co_3O_4/0.5at%Ni samples for (p) H_2 and (q) H_2O_2 production without a sacrificial agent under UV-visible light. (r) EPR responses of the DMPO–OH spin adduct in TiO_2/5at%Co_3O_4/0.5at%Ni.[71]

derivative.[82] Utilizing a TiO_2–Ti_3C_2-ZIF-67 mixture, Zhao and co-workers synthesized a TiO_2–Ti_3C_2–CoS_x heterostructure through a solvothermal process, with varying amounts of Ti_3C_2 for hydrogen production.[85] The HER was performed in a Pyrex flask using a 300 W xenon arc lamp, and the highest activity observed was 9500 μmol g^{-1} h^{-1} for the TiO_2–Ti_3C_2–CoS_x with 0.5% Ti_3C_2, showing a better performance over the TiO_2–Ti_3C_2, TiO_2–CoS_x and pristine TiO_2 catalysts.[85]

Porous ternary TiO_2/Co_3O_4/Ni heterojunction was fabricated by Li *et al.* for photocatalytic hydrogen production using bimetallic MOFs, MIL-125/ZIF-67 (Fig. 6).[71] Their studies indicated that the photocatalytic activity of the MOF SC was dependent on the concentration of Co_3O_4 and the Ni loading. The highest hydrogen evolution measured was 27 mmol g^{-1} h^{-1} observed for TiO_2/5at%Co_3O_4/0.5at%Ni containing 5% Co_3O_4. The high performance of the composite was attributed to the interaction between Co_3O_4 and Ni, which promoted the optical-response ability and surface water oxidation kinetics, facilitating the fast transport and utilization of the photo-excited electrons.[71]

Hussain *et al.* synthesized a TiO_2/Cu_xO/C p–n multi-heterostructure from bimetal MOF, MIL-125-NH_2/Cu (Fig. 7). The TiO_2/Cu_xO/C was synthesized by loading Cu into the MOF crystals, followed by one-step carbonization under argon by varying the temperature, leading to the formation of different Cu-charged species.[57] The derived heterojunctions were embedded in a porous carbon matrix, which retained the disc-like morphology inherited from the NH_2-MIL-125(Ti/Cu) precursor. However, they found that the TiO_2/Cu_xO/C formed at 700 °C showed a superior H_2 evolution activity with 3298 μmol g^{-1} h^{-1}. The high performance of TiO_2/Cu_xO/C was attributed to the well-crystalline anatase and rutile TiO_2 phases in the matrix, the formation of a type-II staggered phase junction, and the formation of a heterostructure between Cu_2O and CuO, which facilitated a faster electron transfer, thus suppressing charge recombination.[57] Using a similar approach, Zhang and co-corkers synthesized a TiO_2/CuO heterostructure which retained the porosity of the parent MOFs MIL-125-NH_2/Cu-BDC.[72] The inherent properties of the derivative resulted in the exceptional catalytic performance observed for the HER, when compared to the derivatives from single-node MOFs and those synthesized by conventional methods. By illuminating the glass vial reactor containing the photocatalytic solution with a 450 nm LED lamp and varying the ratio of Cu to Ti in the presence of $[Ru(bpy)_3]^{2+}$ as a photosensitizer, they observed an enhanced HER performance of 19 036 μmol g^{-1} for the 0.4 : 1 molar ratio Cu : Ti, which decreased with further increase of the concentration of Cu. Their results also showed that the TiO_2/CuO was stable, generating over 106 519 μmol g^{-1} H_2 after 24 h.[72]

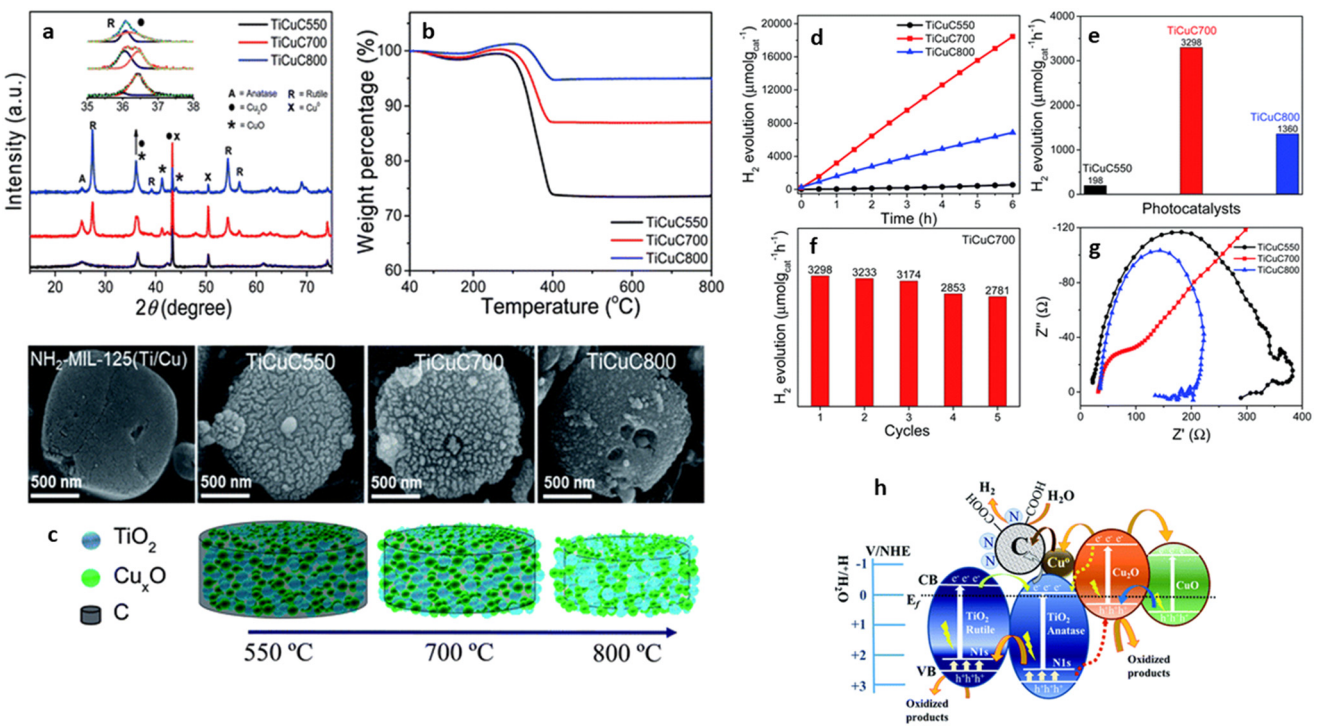

Fig. 7 (a) Powder X-ray diffraction patterns, (b) TGA in air, and (c) SEM images representative schematic diagrams of bi-MOF NH_2-MIL-125(Ti/Cu) derived nanocomposites TiCuC550, TiCuC700 and TiCuC800 obtained at pyrolysis temperatures of 550, 700 and 800 C respectively. (d) Photocatalytic H_2 evolution performance of samples change with the reaction time; (e) comparison of photocatalytic H_2 evolution in μmol g_{cat}^{-1} h^{-1} of TiCuC550 (black), TiCuC700 (red) and TiCuC800 (blue); (f) the recyclability test of the selected TiCuC700 nanocomposite and (g) EIS Nyquist plots of TiCuC550, TiCuC700, and TiCuC800 at the same potential in 0.5 M H_2SO_4, (h) the schematic illustration of the proposed mechanism of photocatalytic H_2 evolution over NH_2-MIL-125(Ti/Cu) derived multi-heterojunction TiCuC700 under UV-vis light MIL-125(Ti/Cu).[57]

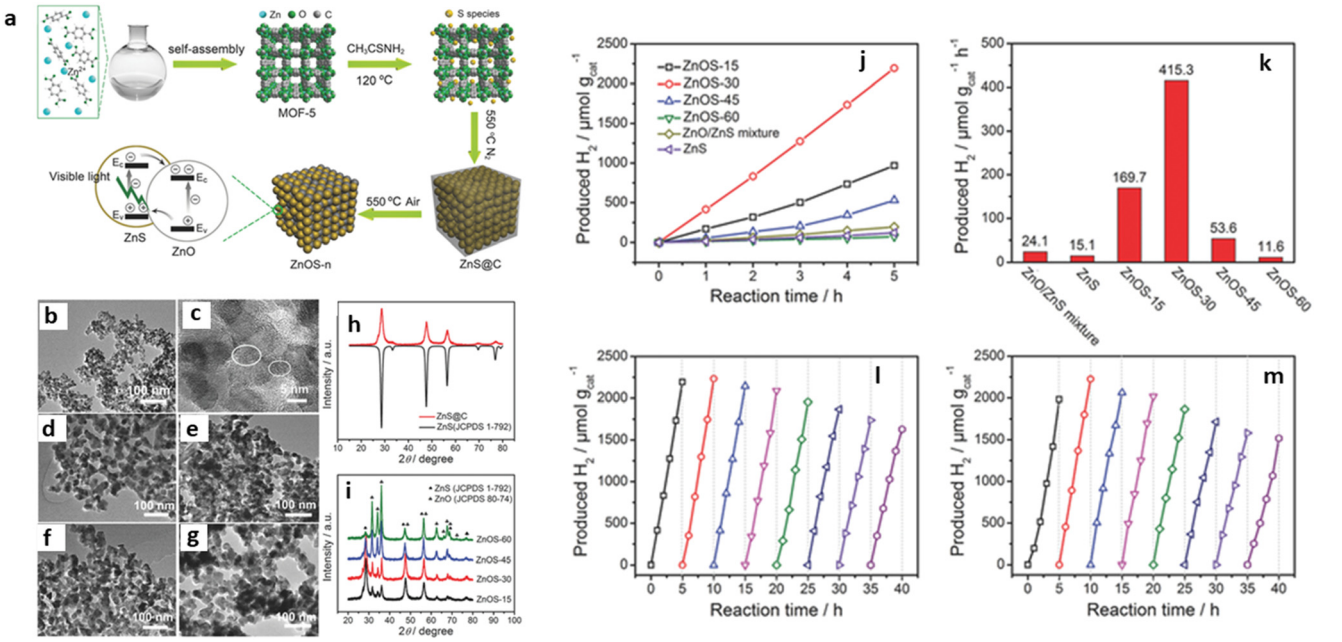

Fig. 8 (a) Schematic illustration of the synthetic procedure of ZnO/ZnS heterostructures. (b) TEM image, (c) HRTEM image, (d) ZnOS-15, (e) ZnOS-30, (f) ZnOS-45, and (g) ZnOS-60. (h) PXRD of ZnS@C. TEM images of (i) PXRD patterns of ZnOS-*n*. The photocatalytic performance of ZnO/ZnS heterostructures. (j) Time-dependent photocatalytic hydrogen evolution under visible-light irradiation ($\lambda > 420$ nm, 300 W Xe lamp) for ZnOS-*n*. (k) Comparison of photocatalytic HER of ZnS/ZnO mixture, ZnS, and ZnOS-*n* under visible-light irradiation. (l) Cycling test of H_2 evolution (evacuation every 5 h) for ZnOS-30 under visible-light irradiation. (m) Cycling test of H_2 evolution (evacuation every 5 h) for recycled and reprocessed ZnOS-30 after 40 h cycling test.[59]

In addition, Zhao *et al.* fabricated different nanostructures of ZnO/ZnS by varying the amount of ZnO using a two-step calcination process, which significantly improved the interfacial catalytic active sites of the MOF-SC (Fig. 8). The photocatalytic solution was irradiated with a 285 nm cut-off optical filter, and the highest evolution rate observed for the best-performing ZnO/ZnS MOF-SC was 415.3 μmol g^{-1} h^{-1}. Their results indicated that the content of ZnO in the heterojunction made it possible to optimize the light absorption capacity and charge separation efficiency, thus improving the performance.[59] Kampouri *et al.* also performed photocatalytic water splitting using MOF-derived mixed-phase TiO_2. Their results indicated that the MOF-derived mixed-phase heterojunction outperformed the single-phase and commercial P25 TiO_2, producing the highest H_2 at the rate of 1394 μmol g^{-1} h^{-1}. They posited that the high H_2 evolution rate observed resulted from the unique morphology that facilitated the constrained contact and distribution of the anatase and rutile phase within the MOF-SC, which resulted in an enhanced synergistic effect, that brought about a significant suppression of the undesired electron–hole recombination.[7]

A 3D open structure, MOF-derived yolk–shell CdS microtube was synthesized by Su *et al.* from Cd–Fe Prussian blue analogues (Cd–Fe-PBA), following an anion exchange and a Kirkendall effect mechanism, through a facile microwave-assisted hydrothermal process.[86] The HER was performed in a quartz reactor using a 300 W xenon lamp coupled with a UV cut-off filter ($\lambda > 420$ nm). They reported the highest activity observed for the MOF-derived yolk–shell CdS with 3051.4 μmol h^{-1} g^{-1}, 2.43 times higher than that of the traditional CdS at 1255.4 μmol h^{-1} g^{-1}. Varying the pH from 4.9 to 13.2 for optimal H_2 production showed that the H_2 evolution rate increased to a maximum at pH 10.8 and declined with an increase in pH above 10.8. Furthermore, their results showed that the MOF-derived yolk–shell CdS demonstrated an enlarged surface area and favorable stability after four cycles, with high photocatalytic activity, owing to an extended visible light response, which enhanced the separation of photogenerated charged species.[86] Recently, Pnictogens such as Bi have also shown promising properties for water splitting owing to their capabilities of forming interphases when combined with co-catalysts. Recently Wei *et al.* synthesized an amorphous and tetragonal $Bi_{0.5}Y_{0.5}VO_4$ solid solutions from a BiYV-MOF under different calcination times of 6, 8, 10, 12, and 16 h at 800 °C using the combined methods of ultrasonication and solvothermal for water splitting (Fig. 9).[87] The photocatalytic reaction was performed in a Pyrex reaction cell using 1% Pt nanoparticles photo deposited on the surface as a co-catalyst and irradiated with a 300 W Xe-lamp. Their observed results indicated that the $Bi_{0.5}Y_{0.5}VO_4$ obtained after 10 h exhibited the best performances on overall water splitting, giving 124.2 μmol h^{-1} g^{-1}. The improved activity of the 10 h $Bi_{0.5}Y_{0.5}VO_4$ was attributed to the thermodynamic property of the catalyst CB and VB positions, coupled with the variation of internal electric field modulating the hetero-phase junction, which created a synchronous relationship between the redox reaction, as well the contribution from the Pt.[87] Chen *et al.* fabricated a core–shell nanostructured Cr_2O_3/C@TiO_2 using

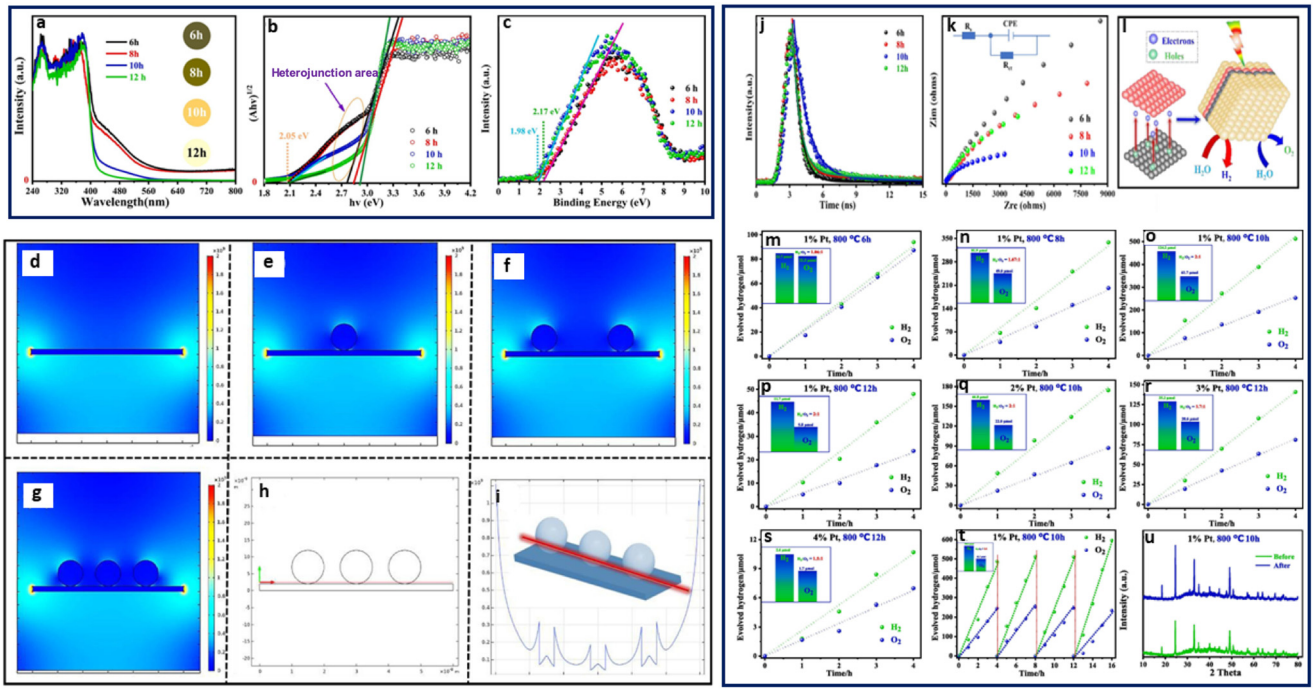

Fig. 9 (a) UV-vis spectrum, (b) energy band, (c) XPS valance band of amorphous and tetragonal $Bi_{0.5}Y_{0.5}VO_4$. Simulated photogenerated electric field distribution after the light irradiation: irradiation on the surface of catalyst (d) without Pt, (e) with Pt particle, (f) with twice the amount of Pt particles (g) with threefold Pt particles, (h) and (i) the intensity of electric field simulation at the same level (red line; the *y*-axis means the intensity in both (e) and (f). (j) Nanosecond time-resolved transient fluorescence decay spectrum, (k) EIS Nyquist plots of the samples, (l) schematic illustration of the enhanced separation of photocarriers *via* the internal electric field, (m)–(s) photocatalytic overall water splitting performance of $Bi_{0.5}Y_{0.5}VO_4$ prepared by MOF-derived method and (t) recycling performance of the material and (u) the XRD results before and after photocatalytic performances.[87]

Mil-101(Cr)/TiF_4 followed by calcination at different temperatures under N_2. The resulting Cr_2O_3/C@TiO_2 composites were labeled MT400, MT500, MT600, and MT700.[88] Results of the photocatalytic reactions performed using a 300 W xenon arc lamp in the presence of methanol showed a H_2 evolution of 446 μmol h^{-1} g^{-1} for MT500 as the best photocatalyst, compared to MT400 with 300 μmol h^{-1} g^{-1} and MT700 with 404 μmol h^{-1} g^{-1}. The activity of the MT500 composite was attributed to its wide visible light response range and efficient separation of photogenerated electron–hole pairs, with contribution from the C deposit imparted by the N_2 calcination atmosphere. To confirm the contribution of the C deposit, the Mil-101(Cr)/TiF_4 template was calcined under air. HER was performed using similar conditions for the MT500 formed under air with no C content. The H_2 evolution showed a low performance with 196 μmol h^{-1} g^{-1}, confirming that the calcination atmosphere also plays a crucial role in the activity of the MOF-SC during photocatalysis.[88]

MOF-SCs for dual-functional photocatalysis

Recently, MOF-SCs have shown high potential as dual-functional photocatalysts. Dual-functional photocatalysis is a promising approach that can simultaneously reduce water to produce hydrogen and oxidize organic molecules. Although MOFs have demonstrated dual functional activity,[11,24,31,44] the use of MOF-SCs in this area is still in its infant stage. By employing the principle of photocatalysis, the oxidation of organic molecules, otherwise referred to as the photodegradation reaction (PDR), can be achieved, as well as the production of hydrogen from water, which is called the hydrogen evolution reaction (HER). It is important to mention that these individual reactions would proceed effectively, given that the holes in VB and electrons in the CB are sufficiently separated. When the PDR and HER occur simultaneously in one system, it is referred to as dual functional photocatalysis (DFP). DFP is considered a suitable process for promoting sustainability as it substitutes toxic sacrificial electron donors for organic molecules, bringing about their oxidation.[89,90] While DFP is considered a suitable approach in principle, how to efficiently utilize the holes and electrons for maximal output is still unclear, as such, it is not devoid of some setbacks. In DFP, the HER is the most exhaustive of the two due to the oxygen evolution reaction (OER), which requires four-electron transfer to overcome the activation energy barrier for water splitting.[91] This causes the HER to proceed in an uphill reaction pathway with a $\Delta G° > 0$, while the PDR, on the other hand, proceeds downhill with $\Delta G° < 0$.[92] Driving a DFP system can pose certain challenges due to (i) the band alignments between the CB and VB of the

MOF SC. This means that to have an efficient DFP, one must carefully consider the position of the CB and VB during the engineering of the MOF SC, more favorably, a type II heterojunction will be much suited for this purpose. (ii) DFP suffers from water regeneration through the back reaction of O_2 and H_2. This is true following that molecular O_2 is required for the PDR, which is an oxic process, while the HER proceeds anoxically.[93,94] Therefore, minimizing the availability of molecular O_2 will be crucial for an effective DFP to prevent water regeneration, which may quench the reaction or reduce the rate at which it proceeds. Using traditional SCs, Kim *et al.* first demonstrated the simultaneous degradation of some organic pollutants (4-chlorophenol, urea, and urine) and H_2 production using a titania-based photocatalyst, modified with dual surface components such as metals and nonmetals. They showed that titania-doped multiple surface components (F–TiO_2/Pt and P–TiO_2/Pt) outperformed the single-doped components (F–TiO_2, P–TiO_2, or Pt/TiO_2) in producing the highest H_2 of over 80 μmol g^{-1} h^{-1} with the concurrent degradation of the organic molecules. They attributed the performance to the synergistic effect of the anions and metal deposits on the surface of TiO_2, which enhanced the interfacial electron transfer, thus reducing the recombination rate of charged species.[89]

In 2017, Zhang *et al.* synthesized a MOS_2 QD-decorated hierarchical assembly of $ZnIn_2S_4$ on reduced graphene oxide as a photocatalyst for wastewater purification and simultaneous H_2 production. The highest activity was recorded for rhodamine blue with a degradation efficiency of 88% and H_2 rate of 45 μmol g^{-1} h^{-1}. Recently, Yan *et al.* improved on Zhang's methods by synthesizing an urchin-like oxygen-doped MoS_2/$ZnIn_2S_4$ composite with a unique microstructure decorated with numerous active sites and charge transfer channels that suppressed charge species recombination. Results from the half HER reaction indicated an efficient H_2 evolution rate of 12.8 mmol g^{-1} h^{-1} (Fig. 10). However, when the DFP was performed, the highest activity was recorded for bisphenol A, with a decomposition efficiency of 53.0% and 672.7 μmol g^{-1} h^{-1} of H_2 produced.[90] The low H_2 rate obtained from the DFP on bisphenol A was, however, not unlikely due to the possible tradeoff in the DFP

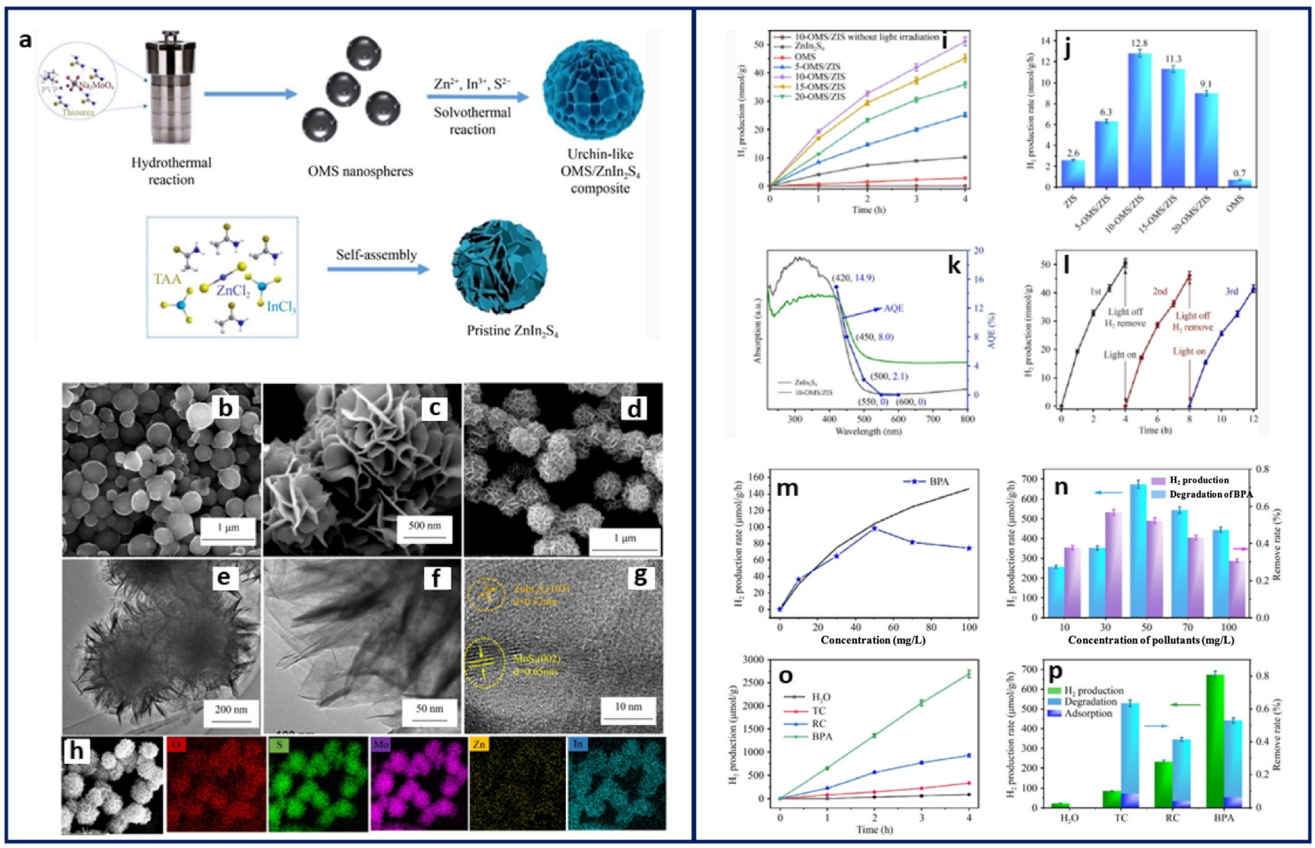

Fig. 10 (a) Schematic showing the fabrication process of OMS/ZIS composite. SEM images of (b) OMS, (c) $ZnIn_2S_4$, and (d) 10-OMS/ZIS. TEM images of 10-OMS/ZIS (e and f) HRTEM image of 10-OMS/ZIS. (g) SEM image of 10-OMS/ZIS, and (h) corresponding elemental mapping images, (i) cycling experiment of HER activity over the as-synthesized samples, (j) comparison of HER rate for the as-synthesized samples under visible light, (k) UV-vis spectra and AQE of $ZnIn_2S_4$ and 10-OMS/ZIS, (l) error bars showing standard deviation three cycle experiments performed with 10-OMS/ZIS. Dependence between the HER rate and BPA concentration using 10-OMS/ZIS (m) blackline indicates Langmuir–Hinshelwood fitting; HER and simultaneous BPA degradation over 10-OMS/ZIS under visible light for 4 h at different concentrations (n) accumulation of H_2 for different pollutants after 4 h. (o) Simultaneous H_2 production and pollutant degradation, and (p) error bar plot showing the standard deviation of three cycle experiments.[90]

process. This suggests that the organic molecule of interest is significant, as its solubility and electron donation ability are crucial to achieving an efficient DFP.

Conclusion and future outlook

MOF-SCs have a high potential for applications in the field of energy and environment, owing to the versatility of the MOF templates, which can be carefully tailored to the derivatives. In this review, we described different elegant strategies in which the properties of MOF-SCs can be tuned for generating hydrogen at high rates. That said, hydrogen production using MOF-SCs suffers from inefficiencies primarily because of the poor light absorption capacity and fast recombination rates of charged species during water splitting, leading to low apparent quantum efficiencies. Therefore, the bulk of the task lies in designing a well-decorated and highly stable photocatalyst that can drive the reaction toward favorable outcomes. The effect of temperature and environment, design of heterojunctions, and engineering of defects have been highlighted as ways to improve the performance of the HER. Additionally, understanding the effect of pH, the presence of reactive oxygen species (ROS), and how they are generated can help design suitable experimental conditions. However, the holes generated during the HER are often left unexploited, and their presence directly or indirectly contributes to slower reaction kinetics since only the electrons are desired for the HER. Therefore, dual-functional photocatalysis for simultaneous hydrogen production and water purification provides a viable alternative approach to best utilize the photocatalytic system, bringing about environmental remediation from water purification and high energy conversion from the H_2 generation. This calls for developing novel materials, such as high-performing MOF-SCs and suitable technologies that can drive the realization of the HER and an efficient DFP.

Conflicts of interest

The authors declare no competing interests.

Acknowledgements

K. C. S. thanks the Department of Chemistry at Oregon State University (OSU) for support through start-up funding. K. C. S. acknowledges Marilyn and Brian Kleiner for their generous support of this project through their donor-advised fund.

References

1 M. Z. Selcuk, M. S. Boroglu and I. Boz, *React. Kinet., Mech. Catal.*, 2012, **106**, 313–324.
2 Y. Li, Y. K. Peng, L. Hu, J. Zheng, D. Prabhakaran, S. Wu, T. J. Puchtler, M. Li, K. Y. Wong, R. A. Taylor and S. C. E. Tsang, *Nat. Commun.*, 2019, **10**, 1–9.
3 F. M. Martínez, E. Albiter, S. Alfaro, A. L. Luna, C. Colbeau-Justin, J. M. Barrera-Andrade, H. Remita and M. A. Valenzuela, *Catalysts*, 2019, **9**, 1–12.
4 Y. Hu, Q. He and C. Xu, *Catalysts*, 2021, **11**, 1455.
5 Hydrogen Production|Department of Energy, **https://www.energy.gov/eere/fuelcells/hydrogen-production**, (accessed 12 October, 2022).
6 D. D. Nguyen, S. I. Ngo, Y. Il Lim, W. Kim, U. Do Lee, D. Seo and W. L. Yoon, *Int. J. Hydrogen Energy*, 2019, **44**, 1973–1987.
7 S. Kampouri, C. P. Ireland, B. Valizadeh, E. Oveisi, P. A. Schouwink, M. Mensi and K. C. Stylianou, *ACS Appl. Energy Mater.*, 2018, **1**, 6541–6548.
8 A. Fujishima and K. Honda, *Nature*, 1972, **238**, 37–38.
9 M. Li, S. Zhang, L. Li, J. Han, X. Zhu, Q. Ge and H. Wang, *ACS Sustainable Chem. Eng.*, 2020, **8**, 11465–11476.
10 N. K. Gupta, Y. Ghaffari, S. Kim, J. Bae, K. S. Kim and M. Saifuddin, *Sci. Rep.*, 2020, **10**, 1–11.
11 S. Kampouri and K. C. Stylianou, *ACS Catal.*, 2019, **9**, 4247–4270.
12 Y. Zhou, L. Zhang and S. Tao, *RSC Adv.*, 2018, **8**, 3433–3442.
13 Y. Zhang, J. Zhou, Z. Li and Q. Feng, *J. Mater. Sci.*, 2018, **53**, 3149–3162.
14 S. Sakthivel, B. Neppolian, M. V. Shankar, B. Arabindoo, M. Palanichamy and V. Murugesan, *Sol. Energy Mater. Sol. Cells*, 2003, **77**, 65–82.
15 S. L. Chiam, S. Y. Pung and F. Y. Yeoh, *Environ. Sci. Pollut. Res.*, 2020, **27**, 5759–5778.
16 H. Li, A. F. Wallace, M. Sun, P. Reardon and D. P. Jaisi, *Environ. Sci. Technol.*, 2018, **52**, 1109–1117.
17 K. Sivula, F. Le Formal and M. Grätzel, *ChemSusChem*, 2011, **4**, 432–449.
18 S. Balachandran and M. Swaminathan, *J. Phys. Chem. C*, 2012, **116**, 26306–26312.
19 J. L. Gomez and O. Tigli, *J. Mater. Sci.*, 2013, **48**, 612–624.
20 L. Shi, Z. Li, T. D. Dao, T. Nagao and Y. Yang, *J. Mater. Chem. A*, 2018, **6**, 12978–12984.
21 C. Dette, M. A. Pérez-Osorio, C. S. Kley, P. Punke, C. E. Patrick, P. Jacobson, F. Giustino, S. J. Jung and K. Kern, *Nano Lett.*, 2014, **14**, 6533–6538.
22 M. Manzoor, A. Rafiq, M. Ikram, M. Nafees and S. Ali, *Int. Nano Lett.*, 2018, **8**, 1–8.
23 C. Prasad, H. Tang, Q. Q. Liu, S. Zulfiqar, S. Shah and I. Bahadur, *J. Mol. Liq.*, 2019, **289**, 111114.
24 X. Zhao, J. Li, X. Li, P. Huo and W. Shi, *Chin. J. Catal.*, 2021, **42**, 872–903.
25 M. Wen, K. Mori, Y. Kuwahara, T. An and H. Yamashita, *Appl. Catal., B*, 2017, **218**, 555–569.
26 B. Zhu, R. Zou and Q. Xu, *Adv. Energy Mater.*, 2018, **8**, 1–33.
27 L. Lu, B. Wu, W. Shi and P. Cheng, *Inorg. Chem. Front.*, 2019, **6**, 3456–3467.
28 G. Capano, F. Ambrosio, S. Kampouri, K. C. Stylianou, A. Pasquarello and B. Smit, *J. Phys. Chem. C*, 2020, **124**, 4065–4072.
29 K. Meyer, S. Bashir, J. Llorca, H. Idriss, M. Ranocchiari and J. A. van Bokhoven, *Chem. – Eur. J.*, 2016, **22**, 13894–13899.
30 M. Yasuda, T. Matsumoto and T. Yamashita, *Renewable Sustainable Energy Rev.*, 2018, **81**, 1627–1635.
31 S. Kampouri, T. N. Nguyen, M. Spodaryk, R. G. Palgrave, A. Züttel, B. Smit and K. C. Stylianou, *Adv. Funct. Mater.*, 2018, **28**, 1–9.

32 K. H. Chu, L. Ye, W. Wang, D. Wu, D. K. L. Chan, C. Zeng, H. Y. Yip, J. C. Yu and P. K. Wong, *Chemosphere*, 2017, **183**, 219–228.
33 Z. H. N. Al-Azri, W. T. Chen, A. Chan, V. Jovic, T. Ina, H. Idriss and G. I. N. Waterhouse, *J. Catal.*, 2015, **329**, 355–367.
34 P. D. Tran, L. Xi, S. K. Batabyal, L. H. Wong, J. Barber and J. S. Chye Loo, *Phys. Chem. Chem. Phys.*, 2012, **14**, 11596–11599.
35 W. Bi, L. Zhang, Z. Sun, X. Li, T. Jin, X. Wu, Q. Zhang, Y. Luo, C. Wu and Y. Xie, *ACS Catal.*, 2016, **6**, 4253–4257.
36 H. Wang, L. Zhang, Z. Chen, J. Hu, S. Li, Z. Wang, J. Liu and X. Wang, *Chem. Soc. Rev.*, 2014, **43**, 5234–5244.
37 S. N. A. Sulaiman, M. Zaky Noh, N. Nadia Adnan, N. Bidin and S. N. Ab Razak, *J. Phys.: Conf. Ser.*, 2018, **1027**, 0–12.
38 R. Asahi, T. Morikawa, T. Ohwaki, K. Aoki and Y. Taga, *Science*, 2001, **293**, 269–271.
39 J. Hu, H. Wang, Q. Gao and H. Guo, *Carbon*, 2010, **48**, 3599–3606.
40 Y. Zhang, J. Xu, J. Zhou and L. Wang, *Chin. J. Catal.*, 2022, **43**, 971–1000.
41 F. Mohammadnezhad, S. Kampouri, S. K. Wolff, Y. Xu, M. Feyzi, J. H. Lee, X. Ji and K. C. Stylianou, *ACS Appl. Mater. Interfaces*, 2021, **13**, 5044–5051.
42 C. W. Huang, V. H. Nguyen, S. R. Zhou, S. Y. Hsu, J. X. Tan and K. C. W. Wu, *Sustainable Energy Fuels*, 2020, **4**, 504–521.
43 S. Subudhi, D. Rath and K. M. Parida, *Catal. Sci. Technol.*, 2018, **8**, 679–696.
44 N.-C. Chiu, M. T. Nord, L. Tang, L. S. Lancaster, J. S. Hirschi, S. K. Wolff, E. M. Hutchinson, K. A. Goulas, W. F. Stickle, T. J. Zuehlsdorff, C. Fang and K. C. Stylianou, *Chem. Mater.*, 2022, **34**, 8798–8880.
45 W. Zhang, Y. Hu, J. Ge, H. L. Jiang and S. H. Yu, *J. Am. Chem. Soc.*, 2014, **136**, 16978–16981.
46 Y. He, Z. Wang, H. Wang, Z. Wang, G. Zeng, P. Xu, D. Huang, M. Chen, B. Song, H. Qin and Y. Zhao, *Coord. Chem. Rev.*, 2021, **429**, 213618.
47 Y. He, X. Zhang, Y. Wei, X. Chen, Z. Wang and R. Yu, *Chem. Res. Chin. Univ.*, 2020, **36**, 447–452.
48 Y. Zhu, K. Yue, C. Xia, S. Zaman, H. Yang, X. Wang, Y. Yan and B. Y. Xia, *Nano-Micro Lett.*, 2021, **13**, 137.
49 X. Liu and J. Song, Metal-organic framework materials for supercapacitors, *J. Phys.: Conf. Ser.*, 2021, **2021**, 12008.
50 R. Krishnapriya, C. Nizamudeen, B. Saini, M. S. Mozumder, R. K. Sharma and A. H. I. Mourad, *Sci. Rep.*, 2021, **11**, 1–12.
51 L. Pan, T. Muhammad, L. Ma, Z. F. Huang, S. Wang, L. Wang, J. J. Zou and X. Zhang, *Appl. Catal., B*, 2016, **189**, 181–191.
52 P. Li, M. Zhang, X. Li, C. Wang, R. Wang, B. Wang and H. Yan, *J. Mater. Sci.*, 2020, **55**, 15930–15944.
53 D. Xu, T. Xia, W. Fan, H. Bai, J. Ding, B. Mao and W. Shi, *Appl. Surf. Sci.*, 2019, **491**, 497–504.
54 Y. Zhou, R. Abazari, J. Chen, M. Tahir, A. Kumar, R. R. Ikreedeegh, E. Rani, H. Singh and A. M. Kirillov, *Coord. Chem. Rev.*, 2022, **451**, 214264.
55 F. Marpaung, M. Kim, J. H. Khan, K. Konstantinov, Y. Yamauchi, M. S. A. Hossain, J. Na and J. Kim, *Chem. - Asian J.*, 2019, **14**, 1331–1343.
56 D. O. Scanlon, C. W. Dunnill, J. Buckeridge, S. A. Shevlin, A. J. Logsdail, S. M. Woodley, C. R. A. Catlow, M. J. Powell, R. G. Palgrave, I. P. Parkin, G. W. Watson, T. W. Keal, P. Sherwood, A. Walsh and A. A. Sokol, *Nat. Mater.*, 2013, **12**, 798–801.
57 M. Z. Hussain, B. van der Linden, Z. Yang, Q. Jia, H. Chang, R. A. Fischer, F. Kapteijn, Y. Zhu and Y. Xia, *J. Mater. Chem. A*, 2021, **9**, 4103–4116.
58 M. Z. Hussain, Z. Yang, B. Van Der Linden, W. R. Heinz, M. Bahri, O. Ersen, Q. Jia, R. A. Fischer, Y. Zhu and Y. Xia, *Energy Fuels*, 2022, **36**, 12212–12225.
59 X. Zhao, J. Feng, J. Liu, J. Lu, W. Shi, G. Yang, G. Wang, P. Feng and P. Cheng, *Adv. Sci*, 2018, **5**, 1700590.
60 B. N. Bhadra, A. Vinu, C. Serre and S. H. Jhung, *Mater. Today*, 2019, **25**, 88–111.
61 R. Das, P. Pachfule, R. Banerjee and P. Poddar, *Nanoscale*, 2012, **4**, 591–599.
62 S. Wang, L. Pan, J. J. Song, W. Mi, J. J. Zou, L. Wang and X. Zhang, *J. Am. Chem. Soc.*, 2015, **137**, 2975–2983.
63 V. E. Henrich, G. Dresselhaus and H. J. Zeiger, *Phys. Rev. Lett.*, 1976, **36**, 1335–1339.
64 P. Behera, S. Subudhi, S. P. Tripathy and K. Parida, *Coord. Chem. Rev.*, 2022, **456**, 214392.
65 S. Dissegna, K. Epp, W. R. Heinz, G. Kieslich and R. A. Fischer, *Adv. Mater.*, 2018, **30**, 1–23.
66 A. Khlyustova, N. Sirotkin, T. Kusova, A. Kraev, V. Titov and A. Agafonov, *Mater. Adv.*, 2020, **1**, 1193–1201.
67 Y. Feng, H. Lu, X. Gu, J. Qiu, M. Jia, C. Huang and J. Yao, *J. Phys. Chem. Solids*, 2017, **102**, 110–114.
68 K. Takanabe, *ACS Catal.*, 2017, **7**, 8006–8022.
69 J. Low, J. Yu, M. Jaroniec, S. Wageh and A. A. Al-Ghamdi, *Adv. Mater.*, 2017, **29**, 1601694.
70 S. Kampouri, F. M. Ebrahim, M. Fumanal, M. Nord, P. A. Schouwink, R. Elzein, R. Addou, G. S. Herman, B. Smit, C. P. Ireland and K. C. Stylianou, *ACS Appl. Mater. Interfaces*, 2021, **13**, 14239–14247.
71 T. Li, J. D. Cui, M. L. Xu, R. Li, L. M. Gao, P. L. Zhu, H. Q. Xie and K. Li, *CrystEngComm*, 2020, **22**, 5620–5627.
72 Y. Zhang, W. Hu, D. Wang, B. J. Reinhart and J. Huang, *J. Mater. Chem. A*, 2021, **9**, 6180–6187.
73 F. Zhao, D. Yin, K. K. Khaing, B. Liu, T. Chen, L. Deng, L. Li, X. Guo, J. Wang, S. Xiao, Y. Ouyang, J. Liu and Y. Zhang, *Inorg. Chem.*, 2020, **59**, 7027–7038.
74 Y. Chen, C. Zhang, X. Zhang, X. Ou and X. Zhang, *Chem. Commun.*, 2013, **49**, 9200–9202.
75 J. Zhang, Z. Zhu and X. Feng, *Chem. – Eur. J.*, 2014, **20**, 10632–10635.
76 X. Hao, Z. Cui, J. Zhou, Y. Wang, Y. Hu, Y. Wang and Z. Zou, *Nano Energy*, 2018, **52**, 105–116.
77 T. Jiang, K. Wang, T. Guo, X. Wu and G. Zhang, *Chin. J. Catal.*, 2020, **41**, 161–169.
78 Y. Pi, S. Jin, X. Li, S. Tu, Z. Li and J. Xiao, *Appl. Catal., B*, 2019, **256**, 117882.
79 K. E. Dekrafft, C. Wang and W. Lin, *Adv. Mater.*, 2012, **24**, 2014–2018.

80 Y. Qi, J. Xu, Y. Fu, C. Wang and L. Wang, *ChemCatChem*, 2019, **11**, 3465–3473.
81 L. Jiang, X. Yuan, Y. Pan, J. Liang, G. Zeng, Z. Wu and H. Wang, *Appl. Catal., B*, 2017, **217**, 388–406.
82 X. Liu, L. Zhang, Y. Li, X. Xu, Y. Du, Y. Jiang and K. Lin, *Mater. Res. Bull.*, 2021, **133**, 111078.
83 J. Liu, X. Zhao, P. Jing, W. Shi and P. Cheng, *Chem. – Eur. J.*, 2019, **25**, 2330–2336.
84 L. Han, F. Jing, J. Zhang, X. Z. Luo, Y. L. Zhong, K. Wang, S. H. Zang, D. H. Teng, Y. Liu, J. Chen, C. Yang and Y. T. Zhou, *Appl. Catal., B*, 2021, **282**, 119602.
85 J. H. Zhao, L. W. Liu, K. Li, T. Li and F. T. Liu, *CrystEngComm*, 2019, **21**, 2416–2421.
86 Y. Su, D. Ao, H. Liu and Y. Wang, *J. Mater. Chem. A*, 2017, **5**, 8680–8689.
87 Z. Wei, Y. Zhu, W. Guo, J. Liu, Z. Jiang and W. Shangguan, *Chem. Eng. J.*, 2021, **414**, 128911.
88 Y. Chen, G. Mao, Y. Tang, H. Wu, G. Wang, L. Zhang and Q. Liu, *Chin. J. Catal.*, 2020, **42**, 225–234.
89 J. Kim, D. Monllor-Satoca and W. Choi, *Energy Environ. Sci.*, 2012, **5**, 7647–7656.
90 T. Yan, Q. Yang, R. Feng, X. Ren, Y. Zhao, M. Sun, L. Yan and Q. Wei, *Front. Environ. Sci. Eng.*, 2022, **16**, 131.
91 Q. Liang, G. Brocks and A. Bieberle-Hütter, *JPhys Energy*, 2021, **3**, 026001.
92 M. Sato and T. Abe, *RSC Adv.*, 2022, **12**, 1850–1854.
93 M. Stylidi, D. I. Kondarides and X. E. Verykios, *Appl. Catal., B*, 2004, **47**, 189–201.
94 H. Park, H. Il Kim, G. H. Moon and W. Choi, *Energy Environ. Sci.*, 2016, **9**, 411–433.